COMPUTATION OF A SINGLE AIRFOIL GUST RESPONSE AND GUST-CASCADE INTERACTION USING THE CE/SE METHOD

Xiao-Yen Wang*, **Ananda Himansu**
Taitech Inc., NASA Glenn Research Center, Cleveland, OH 44135
*email: xiao-yen.wang@grc.nasa.gov
Sin-Chung Chang and **Philip C.E. Jorgenson**
NASA Glenn Research Center, Cleveland, OH 44135

ABSTRACT

The problems 1 and 2 in Category 3 are solved using the space-time conservation element and solution element (CE/SE) method. Problem 1 concerns the acoustic field generated by the interaction of a convected harmonic vortical gust with a single isolated airfoil. Problem 2 models rotor-stator interaction in a 2D cascade. Both problems involve complex geometries and flow physics including vortex shedding and acoustic radiation. An unstructured triangular mesh is used to solve both problems. For problem 2, the Giles approach is incorporated with the CE/SE method to handle non-equal pitches of the rotor and stator. Numerical solution of both near and far fields of problem 1 are presented and compared with a frequency-domain solver GUST3D and a time-domain high-order Discontinuous Spectra Element Method (DSEM) solutions. For problem 2, numerical solutions on the blade surface, inlet and outlet planes are presented.

1. INTRODUCTION

The method of space-time conservation element and solution element (abbreviated as the CE/SE method) is a finite volume method with second-order accuracy in both space and time. The flux conservation is enforced in both space and time instead of space only. It has low numerical dissipation and dispersion errors. It uses simple non-reflecting boundary conditions and is compatible with unstructured meshes. It is simple, flexible, and generate reasonably accurate solutions. The CE/SE method has been successfully applied to solve numerous practical problems, especially aeroacoustic problems. Details of the numerical algorithm based on the CE/SE method are referred to [1-4]. Applications of the CE/SE method to Computational AeroAcoustic (CAA) problems are referred to [5-10].

2. CATEGORY 3: PROBLEM 1

Consider a Joukowski airfoil in a two-dimensional gust. The geometry of the Joukowski airfoil and mean flow conditions can be found in [11]. The incoming gust has velocity fluctuations described as follows:

$$u' \stackrel{\text{def}}{=} -(v_g\, k_y/|\mathbf{k}|)\cos(k_x x + k_y y - \omega t) \tag{1}$$

$$v' \stackrel{\text{def}}{=} (v_g\, k_x/|\mathbf{k}|)\cos(k_x x + k_y y - \omega t) \tag{2}$$

and

$$\rho' \stackrel{\text{def}}{=} 0 \quad \text{and} \quad p' \stackrel{\text{def}}{=} 0 \tag{3}$$

where (i) $v_g = 0.02, \text{and} k_x = k_y = 0.1, 1.0, 3.0$, (ii) $|\mathbf{k}|$ is the absolute value of $\mathbf{k} = (k_x, k_y)$, i.e.,

$$|\mathbf{k}| \stackrel{\text{def}}{=} \sqrt{k_x^2 + k_y^2} \tag{4}$$

and (iii)

$$\omega = \overline{u}_\infty k_x \tag{5}$$

with $\overline{u}_\infty$ being the mean x-velocity at infinity.

The solution procedure and initial and boundary conditions used in solving this problem are referred to [9] and will not repeated here due to limited space. A 2D parallel CE/SE nonlinear Euler solver is used

in the computation. The parallelization of the CE/SE code is referred to [12]. In the following, numerical results will be presented for both symmetric and cambered airfoils at three gust frequencies.

2.1 Numerical Results of Problem 3.1

In the following subsections, the RMS pressure on the airfoil surface, and the sound intensity at one and four chord lengths from the origin, are presented in the following for all cases to examine both the near and far field solutions. In all figures, the numerical solution of the acoustic pressure non-dimensionalized by v_g is plotted.

2.1.1 Symmetric Airfoil

The symmetric Joukowski airfoil of 12% thickness is analyzed to show the geometrical capability of the CE/SE method. As shown in Fig. 1, the airfoil is surrounded by an unstructured mesh (Fig. 1(a)) which, in turn, is embedded in a triangulated structured mesh (Fig. 1(b)). The unstructured mesh is generated using the code TRUMPET [13]. The mean pressure on the airfoil surface is plotted in Fig. 2 and compared with the potential code FLO36 solutions. The corresponding acoustic solutions are shown in Figs. 3–5 for the three frequencies. A reasonable agreement between CE/SE and GUST3D solutions is observed for $k_x = k_y = 0.1$ and 1.0, while there are discrepancies at $k_x = k_y = 3.0$. However, the CE/SE solutions agree well with the DSEM solution at the far field for $k_x = k_y = 3.0$(Fig. 5(c)).

As an example, a computational domain of $-23 \leq x, y \leq 23$ is used for $k_x = k_y = 3.0$. An unstructured mesh with 7392 triangles is used in the region of $-2 \leq x, y \leq 2$ while a uniform triangulated structured mesh formed from 420000 triangles is used in the rest of the computational domain. On the airfoil surface, there are 168 cells. The RMS pressure solution converges by $t = 10T$ (14000 marching steps). The computation takes 1.5 hours wall-clock-time using 16 CPUs on a SGI Origin 2000 system with 400 MHz MIPS R12000 processors.

2.1.2 Cambered Airfoil

The airfoil considered here has the same thickness as the symmetric airfoil but with a camber ratio of 0.02 and an angle of attack of 2°. The steady lift is no longer zero and the flow field is more complex. A larger computational domain is necessary. As an example, a computational domain of $-40 \leq x, y \leq 40$ is used for the case $k_x = k_y = 1.0$. Among the 643744 triangular cells that fill the entire computational domain, 5344 cells are contained in the region of $-2 \leq x, y \leq 2$ (see Fig. 6). There are 168 points on the airfoil surface. The numerical results are obtained assuming $\Delta t = T/1050$.

The computed mean pressure on the airfoil surface is plotted in Fig. 7 with the FLO36 solution, showing that the CE/SE pressure solution on the upper surface is slightly under-predicted. For the two frequencies $k_x = k_y = 0.1$ and 1.0, the unsteady solutions are plotted in Figs. 8–9, respectively. The CE/SE solutions are very close to the GUST3D solution at $k_x = k_y = 0.1$. However larger discrepancies are observed at $k_x = k_y = 1.0$. The CE/SE solution gives reasonably good agreement with the DSEM solution at $k_x = k_y = 1.0$.

The domain size study is performed for the cambered airfoil at $k_x = k_y = 1.0$. The near field solutions, including the RMS pressure on the airfoil surface and the sound intensity at one chord length, obtained in a smaller domain of $-23 \leq x, y \leq 23$, are identical to the solution presented above. The sound intensity at four chord lengths is slightly different from the presented solution. The non-reflecting boundary condition has some reflections that are generated at the far-field boundary, which is also observed in the RMS pressure contour plot. However the reflection is generally less than 5% of the maximum value of the acoustic field and has little effect on the accuracy of the numerical solutions.

Grid refinement study is not performed because the mesh used in the computation is fine enough to capture both the acoustic waves and the gust. About 30–40 mesh points per wave length are necessary for the CE/SE method since it is 2nd order accurate. In the current computation, about 40 mesh points per wave length are used.

3. CATEGORY 3: PROBLEM 2

Consider the rotor-stator interaction problem. The wake generated by the rotor blade at the upstream of the stator is described as follows:

$$u'_g = \sum_{n=1}^{3} a_n \cos[n(k_y y - \omega t)] \cos\beta \tag{6}$$

$$v'_g = -u'_g \tan\beta \tag{7}$$

where $k_y = 11\pi/9, \omega = 3\pi/4, \beta = 44°, a_1 = 5\text{x}10^{-3}, a_2 = 3\text{x}10^{-3}$, and $a_3 = 7\text{x}10^{-4}$. And $n = 1, 2, 3$ corresponds to the rotor blade passing frequency (BPF) and its harmonics. Assume the pitches of the rotor and stator be P_r and P_s. Then $P_r = 2\pi/k_y = 18/11$, while $P_s = 2/3$ is given. The ratio of the rotor and stator pitches, $P_r/P_s(=27/11)$, is not unity. In order to impose the periodic boundary condition in the y- direction, 27 passages of the stator vane has to be used in the computation, which is very expensive. An approach to treat non-equal pitches was developed by Giles in [14] for the analysis of rotor/stator interaction. The same approach is adopted in the space-time CE/SE method in this work. In the following, the Giles approach and its validation will be described briefly, which is followed by the numerical results of the benchmark problem.

3.1 Non-equal Pitch Treatment and its Validations

Consider the 2D nonlinear Euler equations described as follows:

$$\frac{\partial u_m}{\partial t} + \frac{\partial f_m}{\partial x} + \frac{\partial g_m}{\partial y} = 0, \quad m = 1, 2, 3, 4 \tag{8}$$

Here

$$u_1 = \rho, \quad u_2 = \rho u, \quad u_3 = \rho v, \quad u_4 = E_t \tag{9}$$

$$f_1 = \rho u,\ f_2 = \rho u^2 + p,\ f_3 = \rho uv,\ f_4 = (E_t + p)u \tag{10}$$

$$g_1 = \rho v,\ g_2 = \rho uv,\ g_3 = \rho v^2 + p,\ g_4 = (E_t + p)v \tag{11}$$

with $E_t = p/(\gamma - 1) + \rho(u^2 + v^2)/2$. By introducing the coordinate transformation:

$$x' = x, \quad y' = y, \quad t' = t - \lambda y \tag{12}$$

where $\lambda = \frac{P_s - P_r}{V P_s}$ with V being the rotor wheel speed, the 2D Euler equations become

$$\frac{\partial (u_m - \lambda g_m)}{\partial t'} + \frac{\partial f_m}{\partial x'} + \frac{\partial g_m}{\partial y'} = 0 \tag{13}$$

Thus the conservation state variables have changed from u_m to $u_m - \lambda g_m$. The numerical scheme for Eq. (13) can be constructed based on the CE/SE method. The time-marching is performed in the x'-y'-t' coordinate. Note that at a constant t', the physical time t is not necessarily the same for different y locations. The periodic boundary condition:

$$u_m(x', y', t') = u_m(x', y' + P_s, t') \tag{14}$$

is imposed at the upper and lower boundaries in the y direction of the computational domain.

The problem 2 in Category 3 of the 2nd CAA Workshop is used here to validate the Giles approach with the CE/SE method. Details of this benchmark problem are referred to [7]. Numerical results obtained by using 4 passages and single passage are presented in Figs. 10–13. When 4 passages are used, the original Euler equations are solved, while the Giles approach is used when the single passage is used in the computation. In this problem, $P_s = 1.0, P_r = 0.8, V = 1.0$, then $\lambda = 0.2$. In Fig. 10, the acoustic pressure contour at one time instance is plotted in the 4 passages to show the wave pattern. In Fig. 11, the acoustic pressure on the upper surface of the flat-plate blade at $y = 0$ is plotted for both solutions obtained by using 4 passages and single passage, showing a good agreement except a slight difference near the leading edge. The RMS pressure at the inlet and outlet planes obtained using 4 passages is plotted in Fig. 12 with the analytical solution, while the corresponding solution obtained using single passage is plotted in Fig. 13, showing slightly better agreement with the analytical solution because of less numerical reflections from the open inlet and outlet boundaries.

3.2 Numerical Results of Problem 3.2

In the current benchmark problem, $P_r = 18/11, P_s = 2/3$, and $V = 27/44$. Due to the numerical stability restriction [14], two passages of the stator vane are used in the computation. Then $\lambda = -10/27$. A mixed triangulated structured and unstructured triangular mesh is used. Approximately 48k triangles exist in the region of $-1.5 \leq x \leq 1.5$ and 300 points define each blade surface. On the blade surface, the slip condition is imposed, i.e., the normal velocity is set to be zero. At the inlet plane, the total pressure, total temperature, and flow angle are specified. The velocity fluctuation (gust) is also imposed. At the outlet, the back pressure is specified, others are extrapolated from neighboring interior points. In the time-marching, the mean flow variables at both the inlet and outlet planes are computed at every time period, T. At the upper and lower boundaries of the computational domain, the periodic boundary condition is imposed. The time step $\Delta t = T/6200$ is used. For one run, it takes around 100T to reach the time periodic state. A Fast Fourier Transform(FFT) analysis in time is performed based on the time-domain solutions to examine the sound pressure level at different BPF ($n = 1, 2, 3$). And a joint FFT analysis in time and spatial y- direction is performed to investigate the sound pressure level as a function of rotor harmonic n, spatial mode order m, and axial location x [15].

The steady-state pressure contour is plotted in Fig. 14. The mean pressure distribution on the blade surface is compared with the Turbo code solution in Fig. 15, showing a good agreement. The sound pressure level versus the rotor harmonic n at the six designated positions on the blade surface, three locations at inlet plane, and three locations at the outlet plane are plotted in Figs. 16 and 17, respectively. It can be seen that the acoustic response exists only at the excitation frequencies ($n = 1, 2, 3$). On the blade surface, the acoustic wave at $n = 1$ is dominant, while at the inlet and outlet planes, the sound pressure level at $n = 2$ becomes the largest. In Fig. 18, the distribution of sound pressure level at different spatial modes along the x- direction is plotted for $n = 1, 2, 3$, respectively. It shows that the spatial modes $m = -32$ and 22 at $n = 1$ exponentially decay, and the spatial modes $m = 10$ at $n = 2$, $m = -42$ and 12 at $n = 3$ propagate both upstream and downstream. Some oscillations are observed in Fig. 18(c), which needs to be investigated further. For $n = 1, 2, 3$, the distribution of sound pressure level on the blade surface, inlet and outlet planes are also plotted in Fig. 19, respectively, to provide a more complete picture of the sound pressure level distribution.

4. CONCLUSIONS

The problems 1 and 2 in Category 3 have been solved using the space-time (CE/SE) method. Numerical results of both problems have been presented. For problem 1, the CE/SE solutions are compared with GUST3D and DSEM solutions. A fairly good agreement between CE/SE and GUST3D solutions at lower frequencies is achieved. There are some discrepancies between CE/SE and GUST3D solution for higher frequencies. However, the CE/SE solution is in good agreement with the DSEM solution for these higher frequencies. For problem 2, no direct comparison between CE/SE and other solutions is made. The CE/SE solutions are similar to the results presented in [15] and agree with the prediction based on the linearized theory [16].

ACKNOWLEDGMENTS

This work was supported by NASA Glenn Research Center through Contract NAS3-97186. The first author would like thank Dr. Jame Scott and Dr. Ed Envia for helpful discussions.

References

[1] S.C. Chang, "The Method of Space-Time Conservation Element and Solution Element – A New Approach for Solving the Navier-Stokes and Euler Equations," *J. Comput. Phys.*, **119,** pp. 295-324, (1995).

[2] S.C. Chang, X.Y. Wang, and C.Y. Chow, "The Space-Time Conservation Element and Solution Element Method – A New High-Resolution and Genuinely Multidimensional Paradigm for Solving Conservation Laws," *J. Comput. Phys.*, **156**, pp. 89–136, (1999).

[3] X.Y. Wang and S.C. Chang, "A 2D Non-splitting Unstructured-triangular-mesh Euler Solver based on the Method of Space-Time Conservation Element and Solution Element," Vol. 8, No. 2, pp. 326-340, 1999, *Computational Fluid Dynamics JOURNAL.*

[4] X.Y. Wang and S.C. Chang, "A 3D Non-splitting Structured/Unstructured Euler Solver based on the Method of Space-Time Conservation Element and Solution Element," AIAA Paper 98-3278, Norfolk, Virginia, June, 1998.

[5] C.Y. Loh, S.C. Chang, J.R. Scott and S.T. Yu, "The Space-Time Conservation Element Method – A New Numerical Scheme for Computational Aeroacoustics," AIAA Paper 96-0276, January 15-18, 1996, Reno, NV.

[6] C.Y. Loh, L.S. Hultgren and S.C. Chang, "Waves Computations in Compressible Flow Using the Space-Time Conservation Element and Solution Element method," *AIAA Journal*, Vol.39, No.5, pp. 794–801, May 2001.

[7] X.Y. Wang, C.Y. Chow and S.C. Chang, "Numerical Simulation of Gust Generated Aeroacoustics in a Cascade Using the Space-Time Conservation Element and Solution Element Method," AIAA Paper 98-0178, January 12-15, 1998, Reno, NV.

[8] X.Y. Wang, S.C. Chang, and P. Jorgenson, "Prediction of Sound Waves Propagating through a Nozzle without/with a Shock Wave Using the Space-Time CE/SE Method," AIAA 2000-0222, Reno, NV, January, 2000.

[9] X.Y. Wang, S.C. Chang, A. Himansu, and P. Jorgenson, "Gust Acoustic Response of a Single Airfoil Using the Space-time Method," AIAA 2002-0801, Reno, NV, January, 2002.

[10] X.Y. Wang, A. Himansu, P. Jorgenson, and S.C. Chang, "Gust Acoustic Response of a Swept Rectilinear Cascade Using the Space-Time CE/SE Method," FEDSM 2001-18134, in *Proceedings of FEDSM'01 2001 Fluids Engineering Summer Meeting*, May 29–June 1, 2001.

[11] The Announcement of the Fourth Computational Aeroacoustics (CAA) Workshop on Benchmark Problems, August, 2003.

[12] A. Himansu, P. Jorgenson, X.Y. Wang and S.C. Chang, "Parallel CE/SE Computations via Domain Decomposition," in *Proceedings of 1st International Conference of Computational Fluid Dynamics*, Kyoto, June, 2000.

[13] P.C.E. Jorgenson and R.H. Pletcher, "An Implicit Numerical Scheme for the Simulation of Internal Viscous Flows on Unstructured Grids," AIAA-94-0306, January 1994.

[14] M. B. Giles, "Generalized Conservation Cells for Finite Volume Calculations," AIAA-87-1118, July, 1987.

[15] S. Sawyer, M. Nallasamy, R. Hixon, R.W. Dyson, L.D. Koch, "Computational Aeroacoustic Prediction of Discrete-Frequency Noise Generated by a Rotor-Stator Interaction," AIAA-2003-3268, May 12–14, 2003.

[16] S.N. Smith, "Discrete Frequency Sound Generation in Axial Flow Turbomachines," Aeronautical Research Council Reports and Memorandum, No. 3709, 1973.

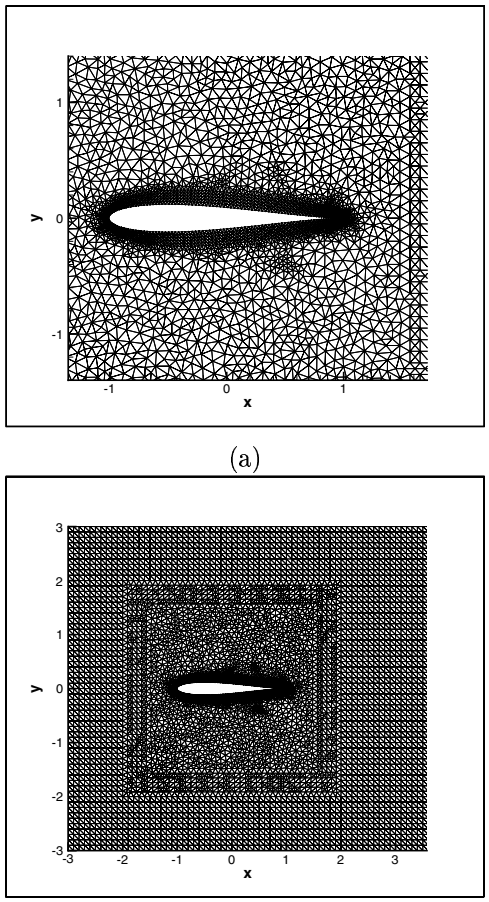

Figure 1: Structured/Unstructured mesh used for the symmetric airfoil calculation.

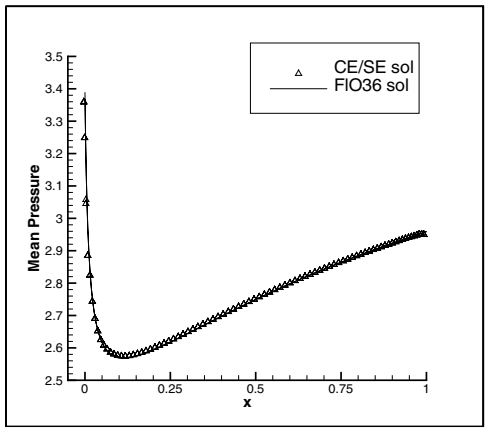

Figure 2: Mean pressure distribution on the airfoil surface for the symmetric airfoil.

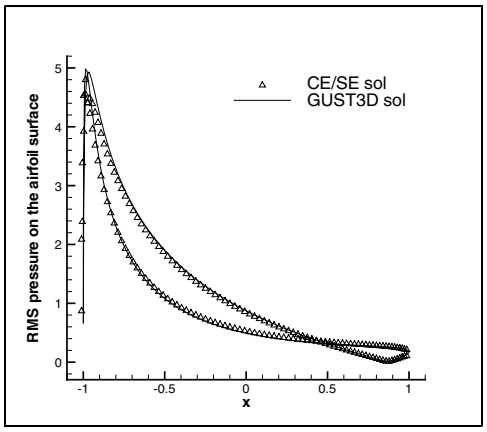

(a) RMS pressure on the airfoil surface.

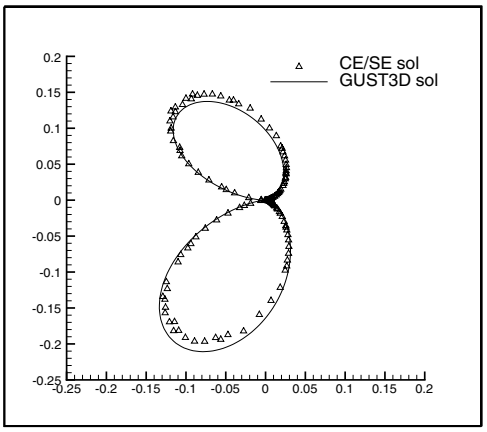

(b) Sound intensity at one chord length.

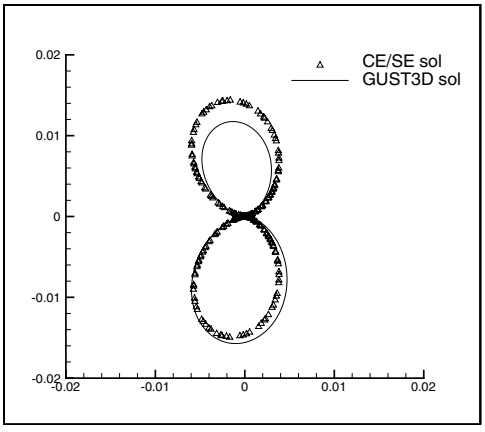

(c) Sound intensity at four chord lengths.

Figure 3: CE/SE solutions for the symmetric airfoil case assuming $k_x = k_y = 0.1$.

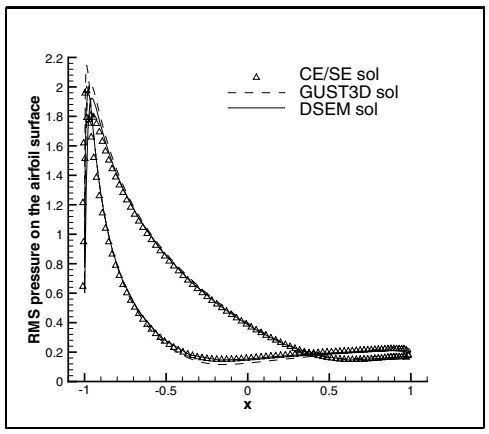

(a) RMS pressure on the airfoil surface.

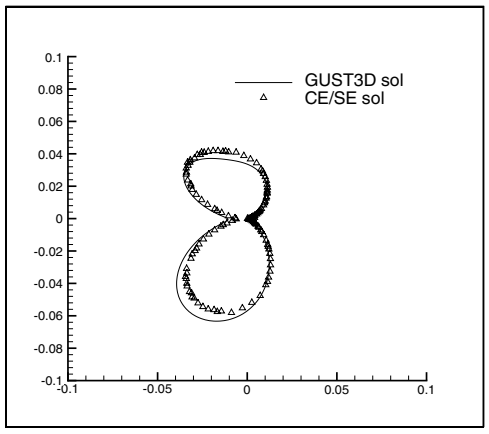

(b) Sound intensity at one chord length.

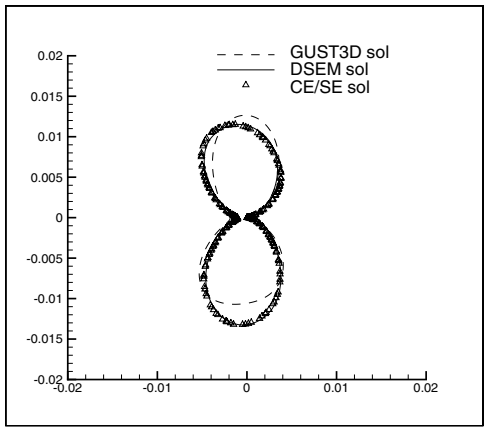

(c) Sound intensity at four chord lengths.

Figure 4: CE/SE solutions for the symmetric airfoil case assuming $k_x = k_y = 1.0$.

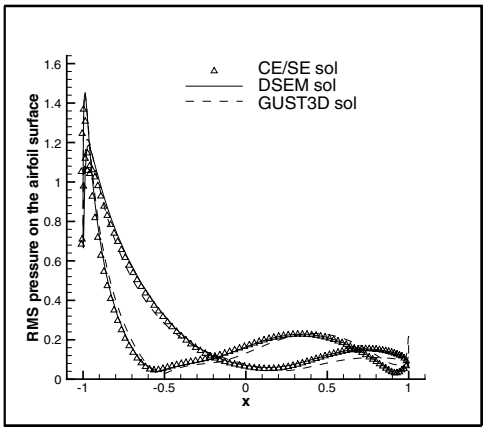

(a) RMS pressure on the airfoil surface.

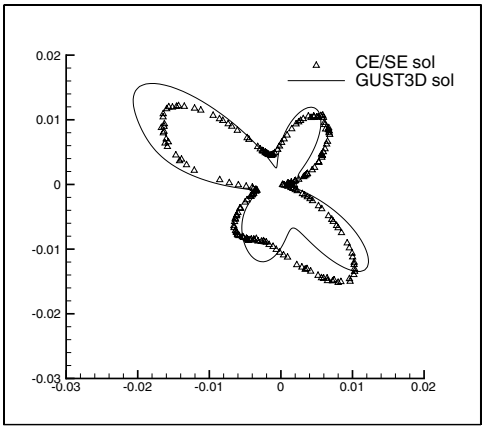

(b) Sound intensity at one chord length.

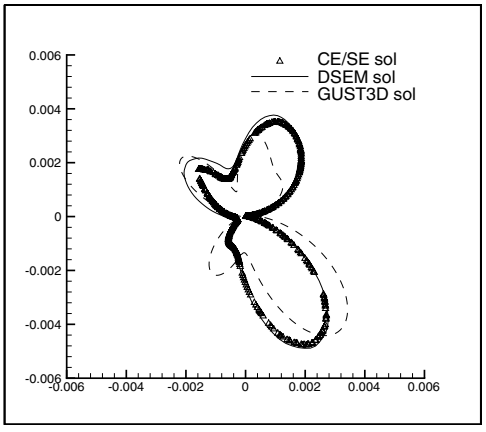

(c) Sound intensity at four chord lengths.

Figure 5: CE/SE solutions for the symmetric airfoil case assuming $k_x = k_y = 3.0$.

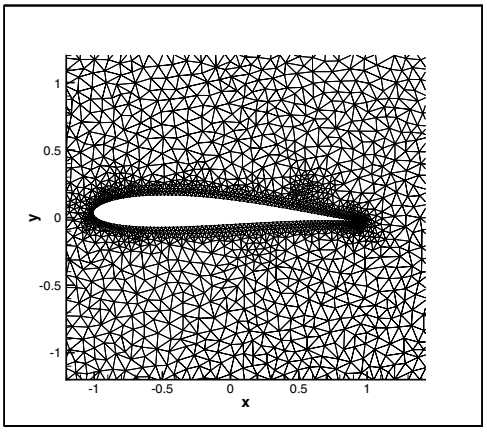

(a)

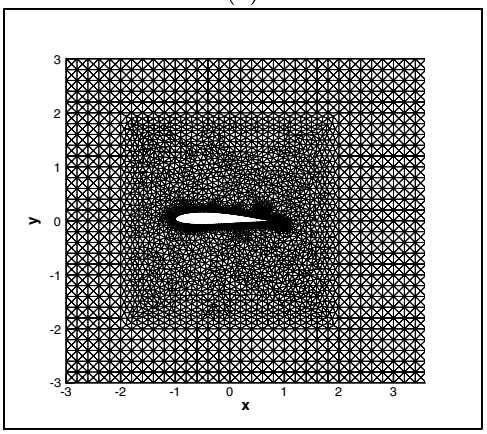

(b)

Figure 6: Structured/Unstructured mesh used in the cambered airfoil calculation.

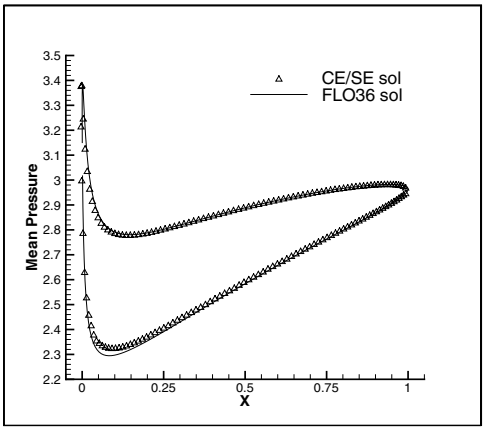

Figure 7: Mean pressure distribution on the airfoil surface for the cambered airfoil.

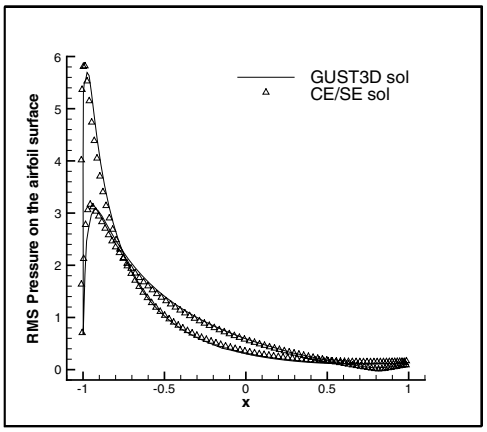

(a) RMS pressure on the airfoil surface.

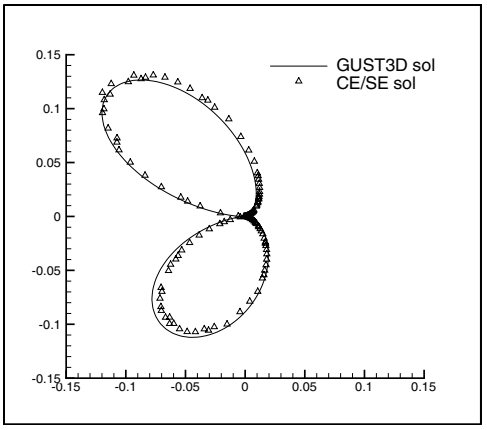

(b) Sound intensity at one chord length.

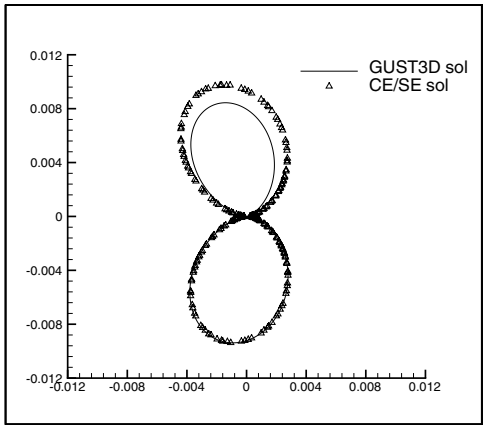

(c) Sound intensity at four chord lengths.

Figure 8: CE/SE solutions for the cambered airfoil case assuming $k_x = k_y = 0.1$.

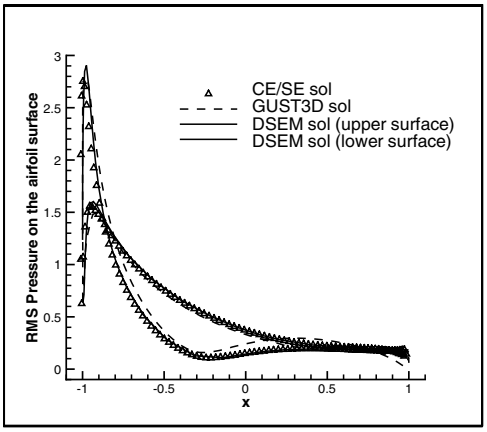

(a) RMS pressure on the airfoil surface.

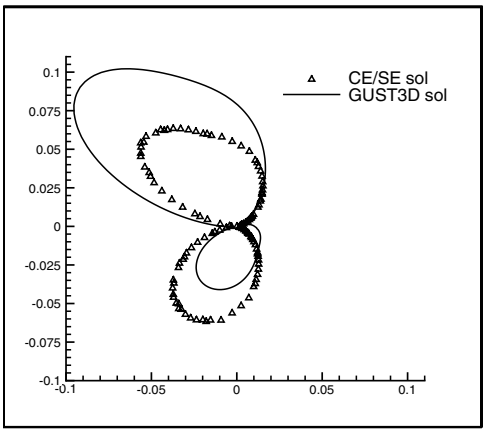

(b) Sound intensity at one chord length.

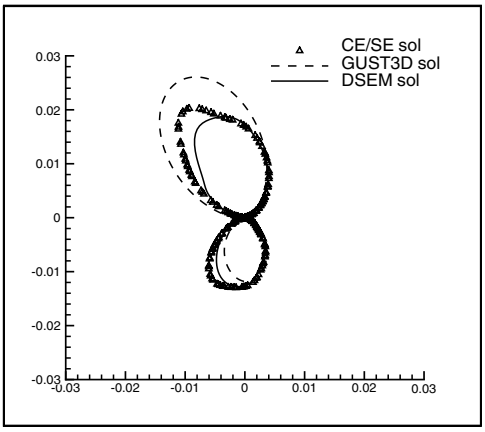

(c) Sound intensity at four chord lengths.

Figure 9: CE/SE solutions for the cambered airfoil case assuming $k_x = k_y = 1.0$.

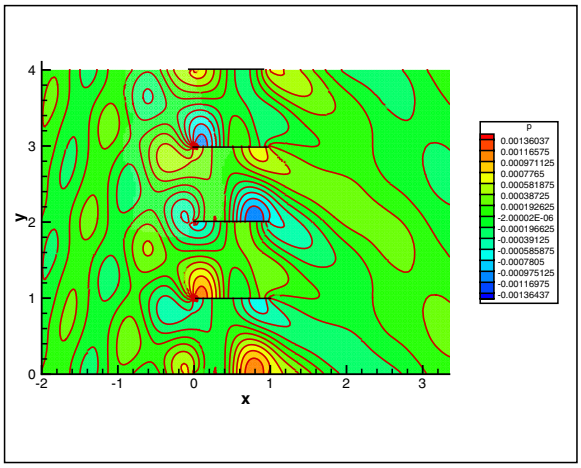

Figure 10: Acoustic pressure contour at one time instance.

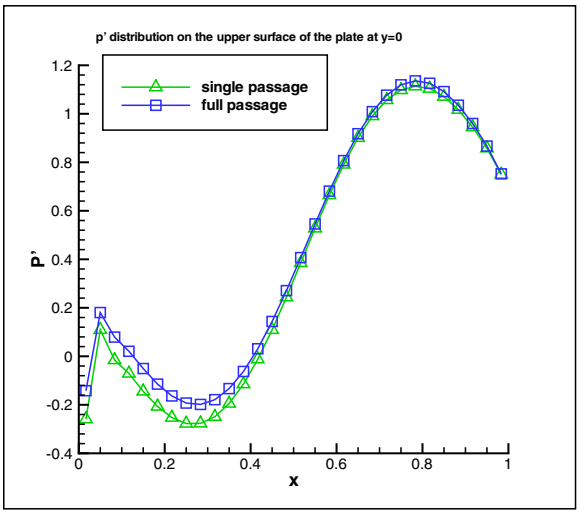

Figure 11: Acoustic pressure distribution on the upper surface of the flat plate located at $y = 0$.

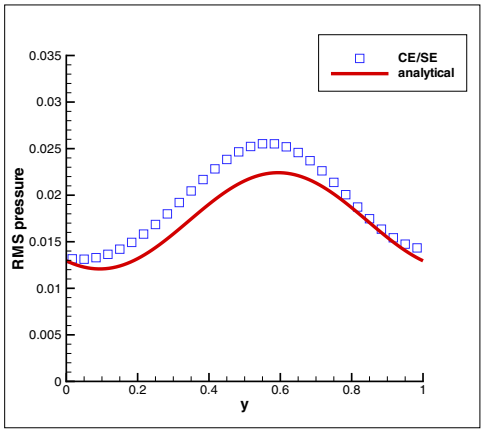

(a) inlet

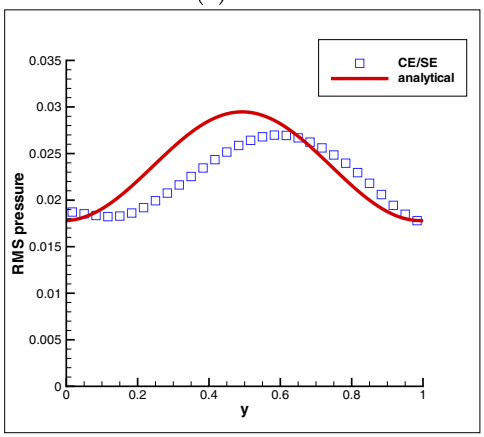

(b) outlet

Figure 12: RMS pressure at the inlet and outlet planes obtained using 4 passages.

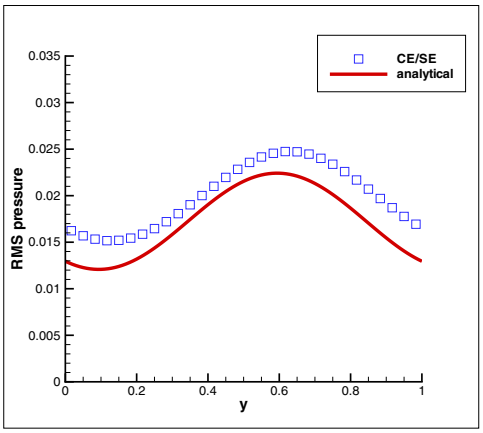

(a) inlet

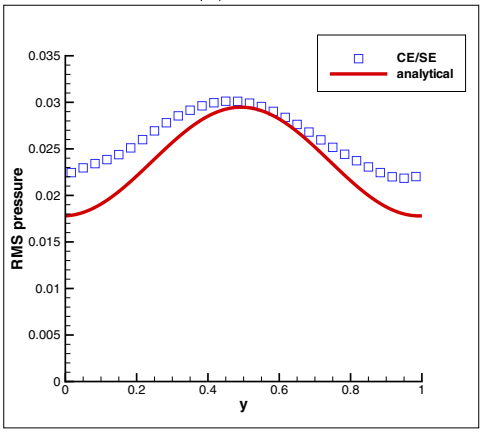

(b) outlet

Figure 13: RMS pressure at the inlet and outlet planes obtained using single passage.

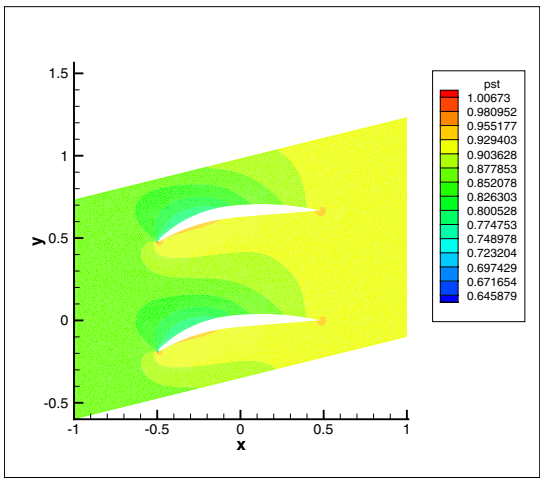

Figure 14: Numerical solution of the mean pressure contours.

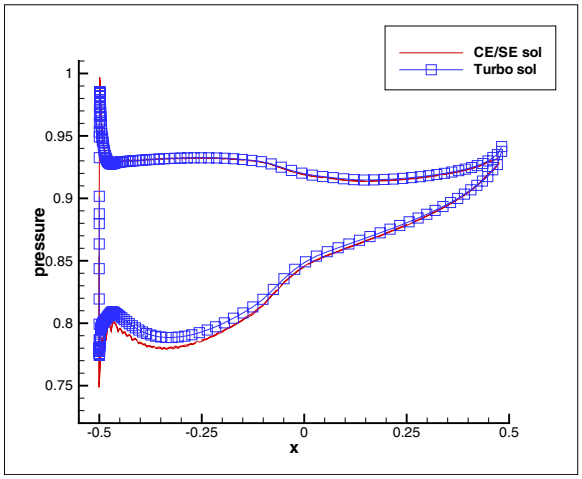

Figure 15: Mean pressure distribution on the blade surface compared with Turbo solution.

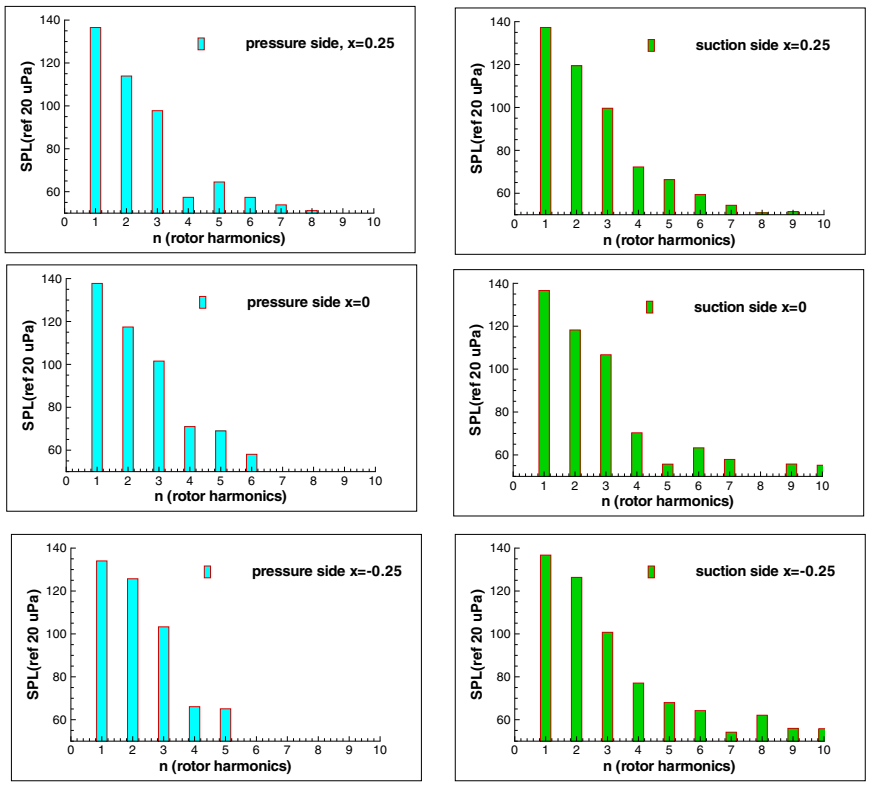

Figure 16: Sound pressure level at six different locations on the blade surface at $n = 1, 2, 3$.

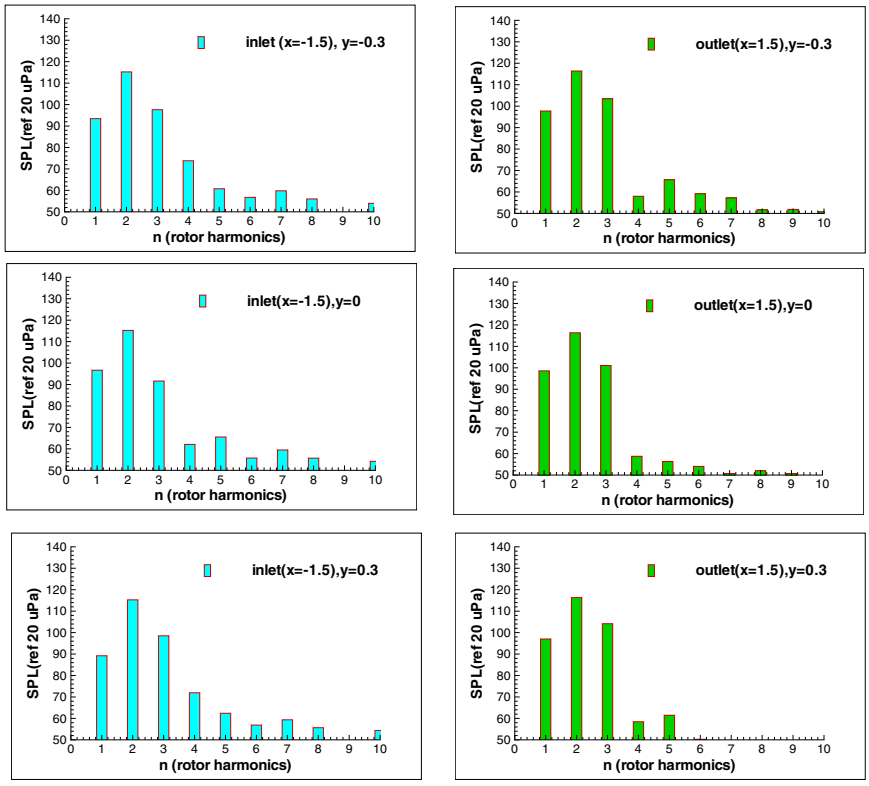

Figure 17: Sound pressure level at three different locations at inlet/outlet planes at $n = 1, 2, 3$.

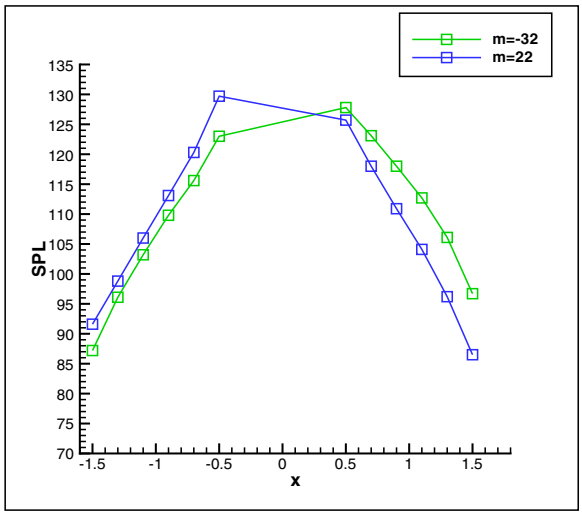

(a) n=1

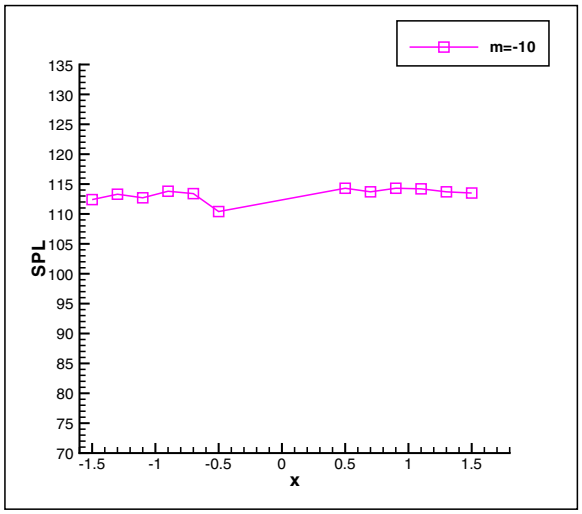

(b) n=2

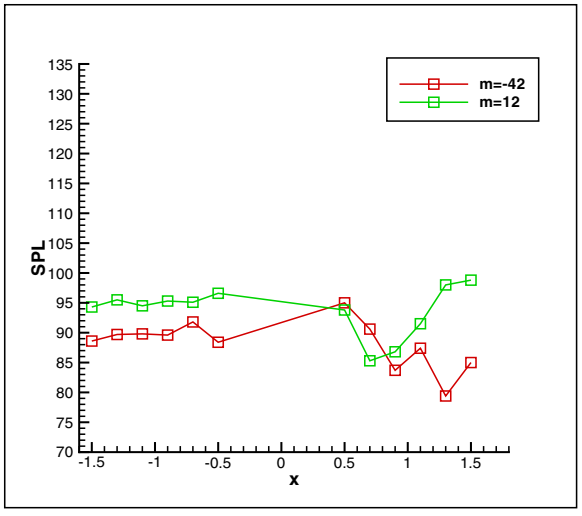

(c) n=3

Figure 18: The distribution of sound pressure level along the cascade for different spatial modes (m) at $n = 1, 2, 3$.

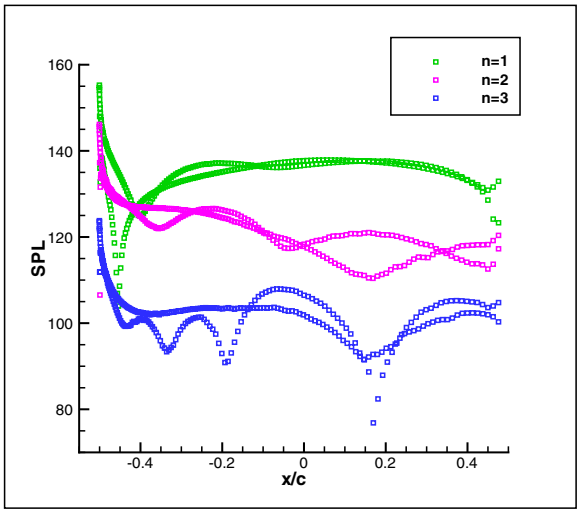

(a) blade surface

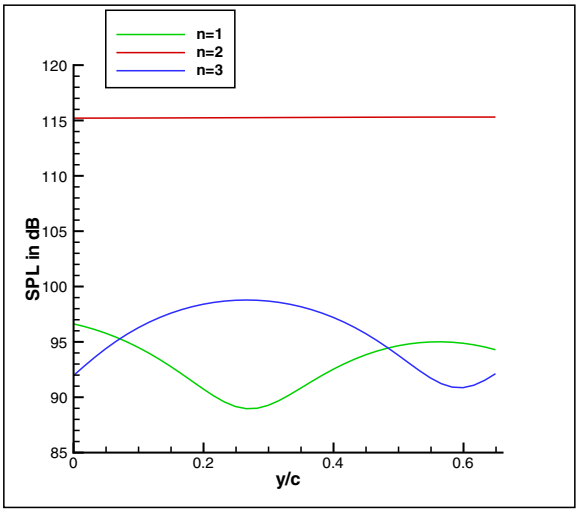

(b) inlet plane

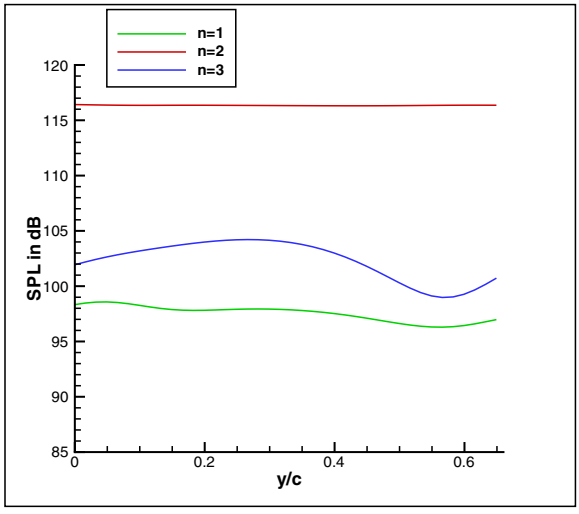

(c) outlet plane

Figure 19: Sound pressure level distribution on the blade surface and at the inlet/outlet planes for $n = 1, 2, 3$.